LIGO: The Laser Interferometer Gravitational-Wave Observatory

The LIGO Scientific Collaboration

The goal of the Laser Interferometric Gravitational-Wave Observatory (LIGO) is to detect and study gravitational waves of astrophysical origin. Direct detection of gravitational waves holds the promise of testing general relativity in the strong-field regime, of providing a new probe of exotic objects such as black hole and neutron stars, and of uncovering unanticipated new astrophysics. LIGO, a joint Caltech-MIT project supported by the National Science Foundation, operates three multi-kilometer interferometers at two widely separated sites in the United States. These detectors are the result of decades of worldwide technology development, design, construction, and commissioning. They are now operating at their design sensitivity, and are sensitive to gravitational wave strains as small as 1 part in 10^{21}. With this unprecedented sensitivity, the data are being analyzed for gravitational waves from a variety of potential astrophysical sources.

The prediction of gravitational waves (GWs), oscillations in the space-time metric that propagate at the speed of light, is one of the most profound differences between Einstein's general theory of relativity and the Newtonian theory of gravity that it replaced. GWs remained a theoretical prediction for more than 50 years until the first observational evidence for their existence came with the discovery of the binary pulsar PSR 1913+16, a system of two neutron stars that orbit each other with a period of 7.75 hours. Precise timing of radio pulses emitted by one of the neutron stars shows that their orbital period is slowly decreasing at just the rate predicted for the general-relativistic emission of GWs (1).

GWs are generated by accelerating aspherical mass distributions. However, because gravity is very weak compared with other fundamental forces, the direct detection of GWs will require very strong sources – extremely large masses moving with large accelerations in strong gravitational fields. The goal of LIGO, the Laser Interferometer Gravitational-Wave Observatory (2) is just that: to detect and study GWs of astrophysical origin. Achieving this goal will mark the

opening of a new window on the universe, with the promise of new physics and astrophysics. In physics, GW detection could provide information about strong-field gravitation, the untested domain of strongly curved space where Newtonian gravitation is no longer even a poor approximation. In astrophysics, the sources of GWs that LIGO might detect (3) include binary neutron stars (like PSR 1913+16 but much later in their evolution); binary systems where a black hole replaces one or both of the neutron stars; a stellar core collapse which triggers a Type II supernova; rapidly rotating, non-axisymmetric neutron stars; and possibly processes in the early universe that produce a stochastic background of GWs.

A GW causes a time-dependent strain in space, with an oscillating quadrupolar strain pattern that is transverse to the wave's propagation direction, expanding space in one direction while contracting it along the orthogonal direction. This strain pattern is well matched by a Michelson interferometer, which makes a very sensitive comparison of the lengths of its two orthogonal arms. LIGO utilizes three specialized Michelson interferometers, located at two sites: an observatory at Hanford, Washington houses two interferometers, the 4 km-long H1 and 2 km-long H2 detectors; and an observatory at Livingston Parish, Louisiana houses the 4 km-long L1 detector. Other than the half-length of H2, the three interferometers are essentially identical. Multiple detectors at separated sites are crucial for rejecting instrumental artifacts in the data, by enforcing coincident detections in the analysis. Also, because the antenna pattern of an interferometer is quite wide, source directions must be located by triangulation using separated detectors.

The initial LIGO detectors were designed to be sensitive to GWs in the frequency band $40-7000$ Hz, and capable of detecting a GW strain amplitude as small as 10^{-21} (2). With funding from the National Science Foundation, the LIGO sites and detectors were designed by scientists and engineers from the California Institute of Technology and the Massachusetts Institute of Technology, constructed in the late 1990s, and commissioned over the first 5 years of this decade. They are now operating at their design sensitivity in a continuous data-taking mode,

and their data are being analyzed for a variety of GW signals by a group of researchers known as the LIGO Scientific Collaboration (4). At the most sensitive frequencies, the instrument strain noise has reached an unprecedented level of 3×10^{-22} rms in a 100 Hz band.

Detector description. It is important to appreciate that the interferometers respond directly to GW amplitude rather than GW power; therefore the volume of space that is probed for potential sources increases as the cube of the strain sensitivity. The challenge is thus to make the instrument as sensitive as possible: at the targeted strain sensitivity of 10^{-21}, the resulting arm length change is only $\sim 10^{-18}$ m, a thousand times smaller than the diameter of a proton.

To increase the interferometer sensitivity, several refinements to the basic Michelson geometry have been made (5), some of which are shown in Fig. 1. First, each arm contains a resonant Fabry-Perot optical cavity, made up of two mirrors that also serve as the gravitational test masses: a partially transmitting mirror (input test mass) and a high reflector (end test mass). These cavities increase the light phase shift for a given strain amplitude, in this case by a factor of 100 for a GW frequency of 100 Hz. Second, another partially transmitting mirror is added between the laser source and the beamsplitter to implement a technique known as power recycling. This takes advantage of the destructive interference at the output port of the beamsplitter (labelled AS, or anti-symmetric port, in Fig. 1), which sends nearly all the power incident on the beamsplitter back towards the laser source. By matching the transmission of the recycling mirror to the optical losses in the Michelson, and resonating this recycling cavity, the laser power stored in the interferometer can be significantly increased. Finally, the two arms are intentionally slightly asymmetric: the path length from the beamsplitter to the input test mass is approximately 30 cm greater in one arm than the other. This is done as part of the readout scheme, as described below.

The laser source is a diode-pumped, Nd:YAG master oscillator and power amplifier sys-

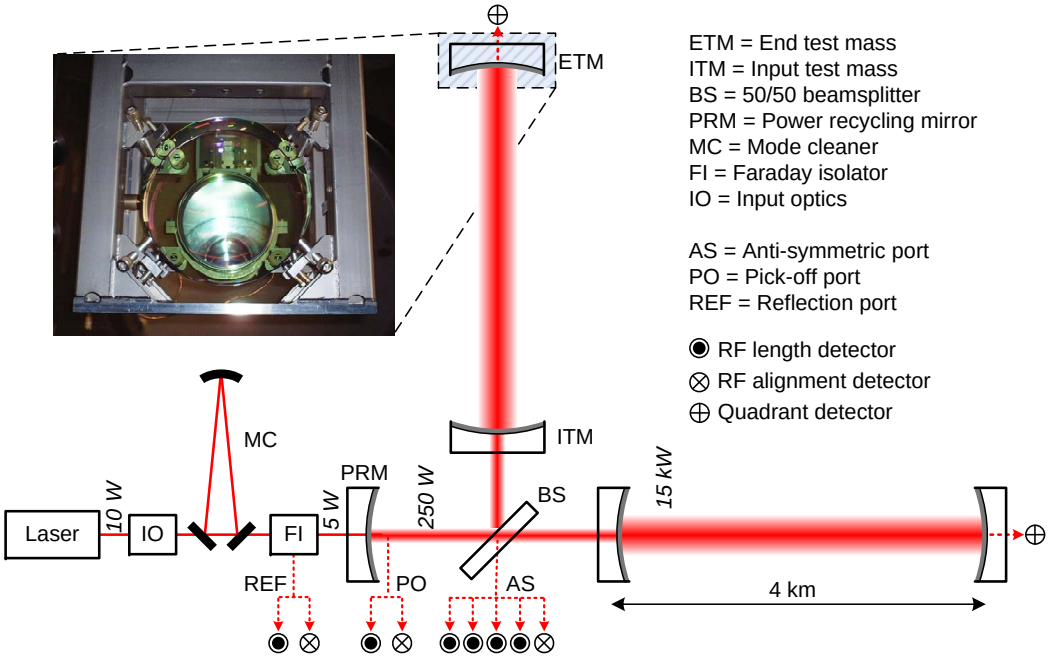

Figure 1: Optical and sensing configuration of the LIGO 4 km interferometers (the laser power numbers here are generic; specific power levels are given in Table 1). The IO block includes laser frequency and amplitude stabilization, and electro-optic modulators. The power recycling cavity is formed between the PRM and the two ITMs, and contains the BS. The inset photo shows an end test mass mirror in its pendulum suspension. The near face is the high-reflecting surface, through which one can see mirror actuators arranged in a square pattern near the mirror perimeter, and optics for handling the transmitted beam behind the mirror.

tem, and emits 10 W in a single frequency, at wavelength 1064 nm (6). The laser amplitude and frequency are actively stabilized (the latter with respect to a reference cavity), and passively filtered with a transmissive ring cavity. The beam is weakly phase-modulated with two radio-frequency (RF) sine waves, producing, to first-order, two pairs of sideband fields around the carrier field; the RF sideband fields are used in a heterodyne detection system to sense the relative positions and angles of the interferometer optics. The beam then passes through an in-vacuum, vibrationally-isolated ring cavity (mode cleaner, MC); the MC provides a stable, diffraction-limited beam, additional filtering of laser noise, and serves as an intermediate reference for frequency stabilization.

Arm length, H1/L1/H2	4000 m / 4000 m / 2000 m
Arm finesse, storage time	220, $\tau_s = 0.95$ msec
Laser type and wavelength	Nd:YAG, $\lambda = 1064$ nm
Input power at recycling mirror, H1/L1/H2	4.5 W / 4.5 W / 2.0 W
Recycling gain, H1/L1/H2	60 / 45 / 70
Arm cavities stored power, H1/L1/H2	20 kW / 15 kW / 10 kW
Test mass size & mass	$\phi 25\mathrm{cm} \times 10\mathrm{cm}$, 10.7 kg
Beam radius ($1/e^2$, H1 and L1), ITM/ETM	3.6 cm / 4.5 cm
Test mass pendulum frequency	0.76 Hz

Table 1: Parameters of the LIGO interferometers. H1 and H2 refer to the interferometers at Hanford, Washington, and L1 is the interferometer at Livingston Parish, Louisiana.

The interferometer optics, including the test masses, are fused-silica substrates with multi-layer dielectric coatings, manufactured to be extremely low-loss. The substrates are polished so that the surface deviation from a spherical figure, over the central 80 mm diameter, is typically 5 angstroms or smaller, and the surface microroughness is typically less than 2 angstroms (7). The absorption level in the coatings is generally a few parts-per-million (ppm) or less (8), and the total scatter loss from a mirror surface is estimated to be 60 – 70 ppm.

The main optical components and beam paths – including the long arms – are enclosed in an ultra-high vacuum system ($10^{-8} - 10^{-9}$ torr) for acoustical isolation and to reduce phase fluctuations from light scattering off residual gas. The 1.2 m diameter beam tubes contain multiple baffles to trap scattered light.

Each optic is suspended as a pendulum by a loop of steel wire. The position and orientation of an optic can be controlled by electromagnetic actuators: small magnets are bonded to the optic and coils are mounted to the suspension support structure, positioned to maximize the magnetic force and minimize ground noise coupling. The pendulum allows free movement of a test mass in the GW frequency band, and provides f^{-2} vibration isolation above its

eigenfrequencies. The bulk of the vibration isolation in the GW band is provided by four-layer mass-spring isolation stacks, on which the pendulums are mounted; these stacks provide approximately f^{-8} isolation above ~ 10 Hz (9). In addition, the L1 detector, subject to higher environmental ground motion than the Hanford detectors, employs seismic pre-isolators between the ground and the stacks. These active isolators employ a collection of motion sensors, hydraulic actuators, and servo controls; the pre-isolators actively suppress vibrations in the band $0.1 - 10$ Hz, by as much as a factor of 10 in the middle of the band (10).

Various global feedback systems maintain the interferometer at the proper working point. For the carrier light, the Michelson interferometer output is operated on a dark fringe, the arm cavities and the power recycling cavity are on resonance, and stringent alignment levels are maintained; these conditions produce maximal power buildup in the interferometer. The RF sideband fields resonate differently. One pair of RF sidebands is not resonant and simply reflects from the recycling mirror. The other pair is resonant in the recycling cavity but not in the arm cavities. The Michelson asymmetry couples most of the power in these sidebands to the anti-symmetric (AS) port. Error signals that determine the proper global operating point are generated by heterodyne detection of the light at the three output ports shown in Fig. 1; single element detectors are used for the length degrees-of-freedom and quadrant detectors are used for the alignment. The controls are implemented digitally, with the photodetector signals sampled and processed at either 16384 samples/sec (length detectors) or 2048 samples/sec (alignment detectors). Feedback signals are applied directly to the optics through their coil-magnet actuators, with slow corrections applied with longer-range actuators that move the whole isolation stack.

Differential disturbances between the arms, including those due to GWs, show up at the AS port. The total AS port power is typically 200 – 250 mW, and is a mixture of RF sidebands, serving as the local oscillator power, and carrier light coming from spatially imperfect interference

at the beamsplitter. The light is divided equally between four length photodetectors, keeping the power on each at a detectable level of 50 – 60 mW. About 1% of the beam is directed to an alignment detector that controls the differential alignment of the ETMs. The four length detector signals are summed and filtered digitally, and the feedback signal is applied differentially to the end test masses. This differential-arm servo loop has a unity-gain bandwidth of approximately 200 Hz, suppressing fluctuations in the arm lengths to a residual level of $\sim 10^{-14}$ m rms.

Common-mode length fluctuations of the arms are essentially equivalent to laser frequency fluctuations, and show up at the reflected port, where photodetection at either RF modulation frequency can be used to detect them. Taking advantage of the high fractional stability of the long arms, this common-mode channel is used in the final level of laser frequency stabilization (11). Feedback is applied to the MC, either directly to a MC mirror position (at low frequencies), or to the error point of the MC servo loop (at high frequencies). The MC servo then impresses the corrections onto the laser frequency. The three cascaded frequency loops – the reference cavity pre-stabilization; the MC loop; and the common mode loop – together provide 160 dB of frequency noise reduction at 100 Hz, and achieve a frequency stability of $5\,\mu$Hz rms in a 100 Hz bandwidth.

The GW channel is the digital error point of the differential-arm servo loop. To calibrate it in strain, the effect of the feedback loop is divided out, and the response to a differential arm strain is factored in (12). The absolute scale is established using the laser wavelength, by measuring the mirror drive signal required to move through an interference fringe. The calibration is tracked during operation with sine waves injected into the differential-arm loop. The uncertainty in the amplitude calibration is approximately $\pm 5\%$. Timing of the GW channel is derived from the Global Positioning System; the absolute timing accuracy of each interferometer is better than $\pm 10\,\mu$sec.

Optimal interferometer alignment is maintained, to within $\sim 10^{-8}$ rad rms per optic, through a hierarchy of feedback loops. Optic orientation fluctuations at the pendulum and first stack eigenfrequencies are suppressed locally at each optic, using optical lever angle sensors. Global alignment is established with four quadrant RF detectors, which together provide linearly independent combinations of the optics' angular deviations from optimal global alignment (13). A multiple-input multiple-output control scheme uses these signals to maintain simultaneous alignment of all angles. Slower servos also hold the beam centered on the optics. In the vertex area this is done using light scattered from the BS face, and at the arm ends with quadrant detectors that receive the leakage through the ETMs.

At full power operation, with 10 – 20 kW in each arm cavity and 200 – 300 W in the recycling cavity, 20 – 60 mW of the beam is absorbed in each ITM, depending on their specific absorption levels. This creates a weak, though not insignificant thermal lens in the ITM substrates, which changes the shape of the optical mode supported by the recycling cavity. The mode shape affects the optical gain, which is optimized for a specific level of absorption in each ITM (approximately 50 mW). To achieve the optimum mode over the range of ITM absorption and stored power levels, each ITM's thermal lens is actively controlled by directing additional heating beams, generated from CO_2 lasers, onto each ITM (14). The power and shape–either a gaussian or annular radial profile–of the heating beams are controlled to maximize the interferometer optical gain and sensitivity.

Instrument performance. During the commissioning period, as the interferometer sensitivity was improved, several short science data-taking runs were made, culminating when the interferometers approached the sensitivity design goal and began the fifth science run (S5) in November 2005. The S5 run will collect full year of coincident interferometer data, lasting until fall of 2007. Since the interferometers detect GW strain amplitude, their performance is typi-

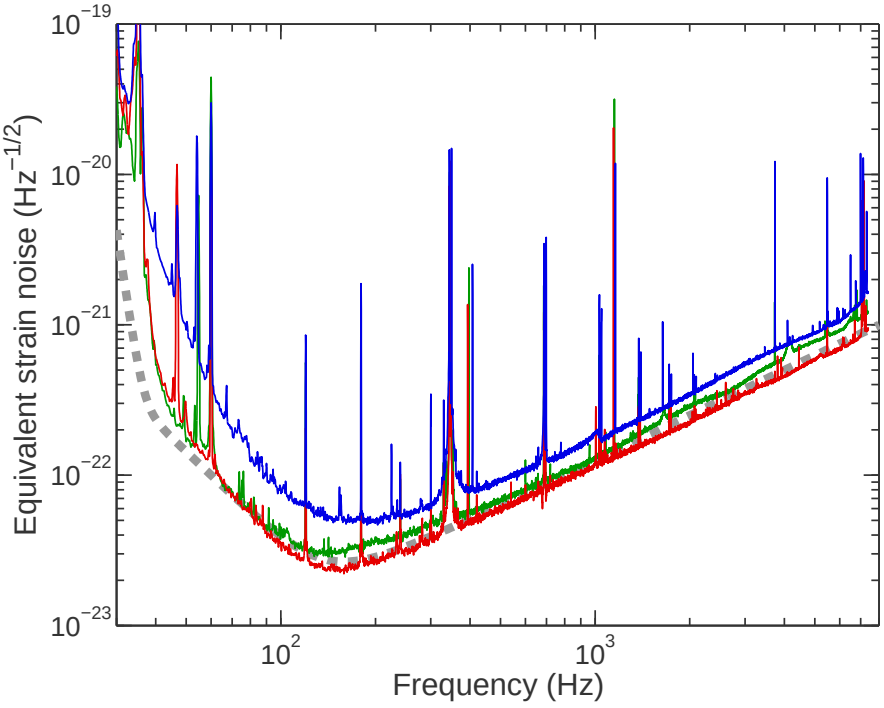

Figure 2: Strain sensitivities, expressed as amplitude spectral densities of detector noise converted to equivalent GW strain. The vertical axis denotes the rms strain noise in 1 Hz of bandwidth. Shown are typical high sensitivity spectra for each of the three interferometers (red: H1; blue: H2; green: L1), along with the design goal for the 4-km detectors (dashed grey).

cally characterized by an amplitude spectral density (the square root of the power spectrum) of detector noise, expressed in equivalent GW strain. Typical high-sensitivity strain noise spectra are shown in Fig. 2. Since the beginning of S5 the strain sensitivity of each interferometer has been improved, by up to 40%, through a series of incremental improvements to the instruments.

The primary noise sources contributing to the H1 strain spectrum are shown in Fig. 3. Understanding and controlling these instrumental noise components has been the major technical challenge in the development of the detectors. The noise terms can be broadly divided into two classes: force noise and sensing noise. Force noises are those that cause motions of the test masses or their mirrored surfaces. Sensing noises, on the other hand, are phenomena that limit

the ability to measure those motions; they are present even in the absence of test mass motion (e.g., in the limit the mirrors had infinite mass).

Sensing noises are shown in the lower panel of Fig. 3. By design, the dominant noise source above 100 Hz is shot noise in the photodetection, as determined by the Poisson statistics of photon detection. The ideal shot-noise limited strain noise density, $\tilde{h}(f)$, for this type of interferometer is (15):

$$\widetilde{h}(f) = \sqrt{\frac{\pi\hbar\lambda}{\eta P_{\rm BS} c}} \frac{\sqrt{1+(4\pi f\tau_{\rm s})^2}}{4\pi\tau_{\rm s}}, \qquad (1)$$

where λ is the laser wavelength, $\hbar$ is the reduced Planck constant, c is the speed of light, $\tau_{\rm s}$ is the arm cavity storage time, f is the GW frequency, $P_{\rm BS}$ is the power incident on the beamsplitter, and η is the photodetector quantum efficiency. For the estimated effective power of $\eta P_{\rm BS} = 0.9 \cdot 250$ W, the ideal shot-noise limit is $\widetilde{h} = 1.0 \times 10^{-23}/\sqrt{\rm Hz}$ at 100 Hz. The shot-noise estimate in Fig. 3 is based on measured photocurrents in the AS port detectors; the resulting value, $\widetilde{h}(100{\rm Hz}) = 1.3 \times 10^{-23}/\sqrt{\rm Hz}$, is higher than the ideal limit due to inefficiencies in the heterodyne detection process.

Many noise contributors are estimated using stimulus-response tests, where a sine-wave or broadband noise is injected into an auxiliary channel to measure its coupling to the GW channel. This method is used for the laser frequency and amplitude noise estimates, the RF oscillator phase noise contribution, and also for the angular control and auxiliary length noise terms described below. Although laser noise is nominally common-mode, it couples to the GW channel through small, unavoidable differences in the arm cavity mirrors (16). For frequency noise, the stimulus-response measurements indicate that the coupling is due to a difference in the resonant reflectivity of the arm cavities of about 0.5%, arising from a loss difference of tens of ppm between the arms. For amplitude noise, the coupling is through an effective dark fringe offset of ~ 1 picometer, due to mode shape differences between the arms.

Force noises are shown in the upper panel of Fig. 3. At the lowest frequencies the largest

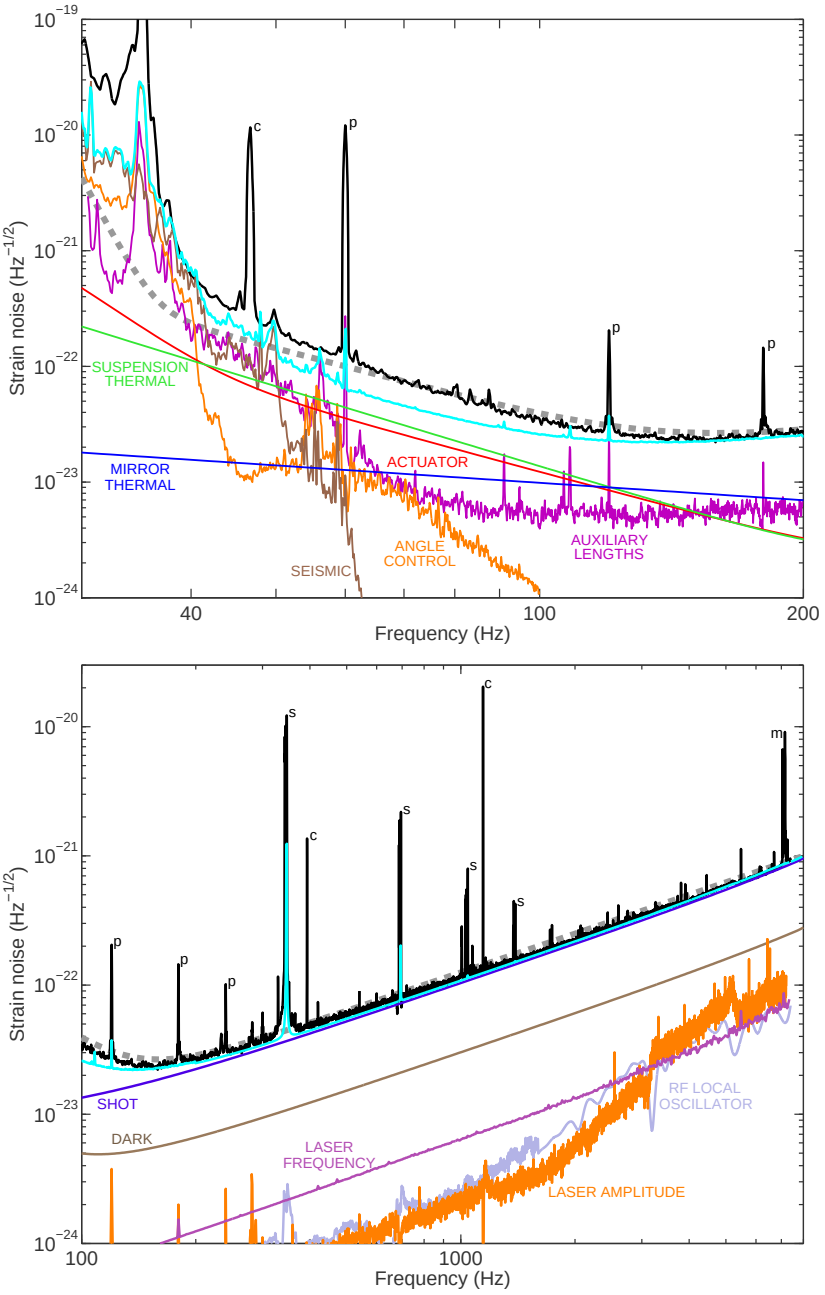

Figure 3: Primary known contributors to the H1 detector noise spectrum. The upper panel shows the force noise components, while the lower panel shows sensing noises (note the different frequency scales). In both panels, the black curve is the measured strain noise (same spectrum as in Fig. 2), the dashed gray curve is the design goal, and the cyan curve is the root-square-sum of all known contributors (both sensing and force noises). The labelled component curves are described in the text. The known noise sources explain the observed noise very well at frequencies above 150 Hz, and to within a factor of 2 in the 40 – 100 Hz band. Spectral peaks are identified as follows: c, calibration line; p, power line harmonic; s, suspension wire vibrational mode; m, mirror (test mass) vibrational mode.

such noise is seismic noise – motions of the earth's surface driven by wind, ocean waves, human activity, and low-level earthquakes – filtered by the isolation stacks and pendulums. The seismic contribution is estimated using accelerometers to measure the vibration at the isolation stack support points, and propagating this motion to the test masses using modeled transfer functions of the stack and pendulum. The seismic wall frequency, below which seismic noise dominates, is approximately 45 Hz, a bit higher than the goal of 40 Hz, as the actual environmental vibrations around these frequencies are ~ 10 times higher than was estimated in the design.

Mechanical thermal noise is a more fundamental effect, arising from finite losses present in all mechanical systems, and is governed by the fluctuation-dissipation theorem (17). It causes arm length noise through thermal excitation of the test mass pendulums (*suspension thermal noise*) (18), and thermal acoustic waves that perturb the test mass mirror surface (*mirror thermal noise*) (19). Most of the thermal energy is concentrated at the resonant frequencies, which are designed (as far as possible) to be outside the detection band. Away from the resonances, the level of thermal motion is proportional to the mechanical dissipation associated with the motion. Designing the mirror and its pendulum to have very low mechanical dissipation reduces the detection-band thermal noise. It is difficult, however, to accurately and unambiguously establish the level of broadband thermal noise *in-situ*; instead, the thermal noise curves in Fig. 3 are calculated from models of the suspension and test masses, with mechanical loss parameters taken from independent characterizations of the materials.

The auxiliary length noise term refers to noise in the Michelson and power recycling cavity servo loops; the former couples directly to the GW channel and latter couples similarly to frequency noise. Above ~ 50 Hz these loops are dominated by shot noise; furthermore, loop bandwidths of ~ 100 Hz are needed to adequately suppress these degrees of freedom, so that the shot noise is effectively added onto their motion. Their noise infiltration to the GW channel,

however, is mitigated by appropriately filtering and scaling their digital control signals and adding them to the differential-arm control signal as a type of feed-forward noise suppression. These correction paths reduce the coupling to the GW channel by 10 – 40 dB.

Angular control noise is minimized by a combination of filtering and parameter tuning. Angle control bandwidths are 10 Hz or less, so low-pass filtering is applied in the GW band. In addition, the angular coupling to the GW channel is minimized by adjusting the relative weighting of the angle control signals sent to the four actuators on each optic, with typical residual coupling levels around 10^{-4} m/rad.

The actuator noise term includes the electronics, starting with the digital-to-analog converters, that produce the coil currents keeping the interferometer locked and aligned. The noise in these circuits is driven largely by the required control ranges; e.g., at low frequency the test mass control range is typically ± 0.4 mrad in angle and $\pm 5\ \mu$m in position.

In the 50 – 100 Hz band, the known noise sources typically do not fully explain the measured noise. Additional noise mechanisms have been identified, though not quantitatively established. Two potentially significant candidates are nonlinear conversion of low frequency actuator coil currents to broadband noise (upconversion), and electric charge build-up on the test masses. A variety of experiments have shown that the upconversion occurs in the magnets of the coil-magnet actuators, and produces a broadband force noise, with a f^{-2} spectral slope. The nonlinearity is small but not negligible given the dynamic range involved: 0.1 mN of low-frequency (below a few Hertz) actuator force upconverts of order 10^{-11} N rms of force noise in the 40 – 80 Hz octave. This noise mechanism is significant primarily below 80 Hz, and varies in amplitude with the level of ground motion at the observatories. Regarding the second mechanism, mechanical contact of a test mass with its nearby mechanical limit-stops, as happens during a large earthquake, can produce electric charge build-up between the two objects. Such charge distributions are not stationary; they will tend to redistribute on the surface to reduce

local charge density. This produces a fluctuating force on the test mass, with an expected f^{-1} spectral slope. The level at which this mechanism currently occurs in the interferometers is not known, but an occurrence on L1, where the strain noise in the 50 – 100 Hz band went down by about 20% after a vacuum vent and pumpout cycle, is attributed to charge reduction on one of the test masses.

In addition to these broadband noises, there are a variety of periodic or quasi-periodic processes that produce lines or narrow features in the spectrum. The sources of most of these spectral peaks are identified in Fig. 3. The groups of lines around 350 Hz, 700 Hz, ... are vibrational modes of the wires that suspend the test masses, thermally excited with kT of energy in each mode. The power line harmonics, at 60 Hz, 120 Hz, 180 Hz ..., infiltrate the interferometer in a variety of ways; the 60 Hz line, e.g., is primarily due to the power line's magnetic field coupling directly to the test mass magnets. As all these lines are fairly stable in frequency, they occupy only a small fraction of the instrument spectral bandwidth.

While Figs. 2 and 3 show high-sensitivity strain noise spectra, the interferometers exhibit both long- and short-term variation in sensitivity due to improvements made to the detectors, seasonal and daily variations in the seismic environment, operational problems, and the like. One indicator of the sensitivity variation over the run is shown in Fig. 4, which histograms the sensitivity of each interferometer to a particular astrophysical source of GWs that is described in the next section: the inspiral of a binary neutron star system. The histogram shows the horizon, which is the maximum distance at which such an event could be detected with good signal-to-noise ratio; this figure-of-merit depends on the detector noise primarily in the band of 70 – 200 Hz. Another significant statistical figure-of-merit is the interferometer duty cycle, the fraction of time that detectors are operating and taking science data. For the period 14 Nov. 2005 to 31 July 2007, the individual interferometer duty cycles were 78%, 78%, and 66% for H1, H2, and L1, respectively; for double-coincidence between Livingston and Hanford the duty cycle

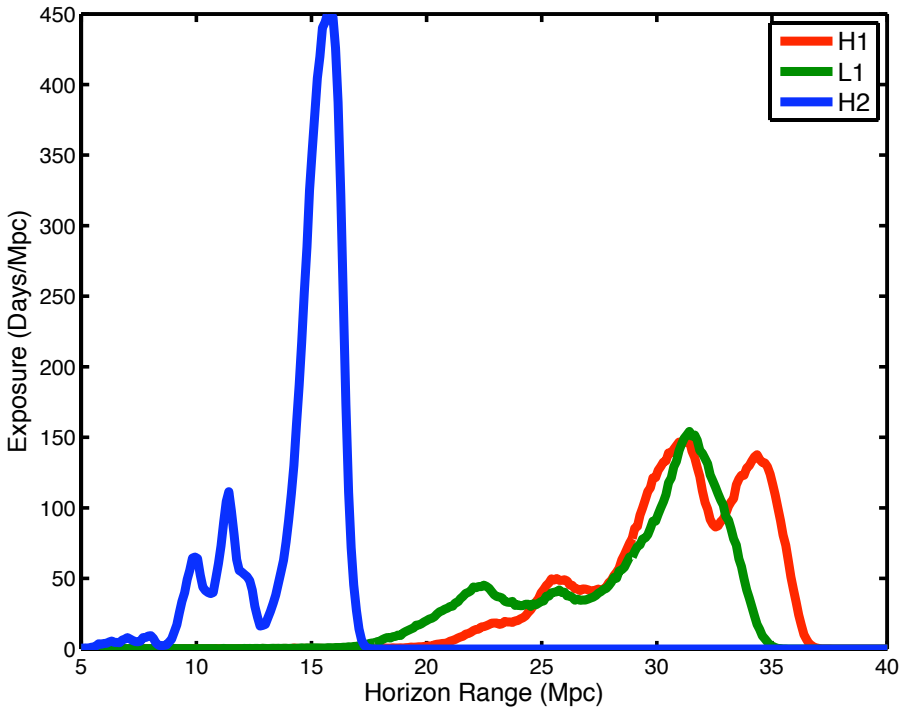

Figure 4: Detection horizon for the inspiral of a double neutron star system (1.4 solar-mass each), for each LIGO interferometer, over the period 14 November 2005 to 31 July 2007. The lower range peaks in each histogram date from the first ~ 100 days of the run, around which time sensitivity improvements were made to all interferometers. Typical range variations over daily and weekly time scales are $\pm 5\%$ about the mean. The range is given in mega-parsecs (Mpc), 3.3 million light years; for reference, the center of the Virgo cluster of galaxies is approximately 16 Mpc from Earth.

was 60%; and for triple-coincidence of all three interferometers the duty cycle was 52%. These figures include scheduled maintenance and instrument tuning periods, as well as unintended losses of operation.

Astrophysical reach. Because there is great uncertainty about the strength and/or rate of occurrence of astrophysical sources of gravitational waves, LIGO was designed so that its data could be searched for GWs from many different sources. Sources can be broadly characterized as either transient or continuous in nature, and for each type, the analysis techniques depend on

	Transient		**Continuous**	
Source Type	Modeled Waveforms	Un-modeled Waveforms	Modeled Waveforms	Un-modeled Waveforms
Examples of sources	Final inspiral binary compact objects	Core collapse supernova, pulsar rotation glitch	Non-axisymmetric neutron stars	Cosmological stochastic background
Astrophysical reach	NS-NS (1.4-1.4 $M_\odot$): 31 Mpc, $250L_{10}$ BH-BH (10-10 $M_\odot$): 125 Mpc, $20,000L_{10}$	$3 \times 10^{-8} M_\odot c^2$ at 10 kpc; $0.1 M_\odot c^2$ at 20 Mpc	$\epsilon \leq 2.3 \times 10^{-6}$ for 200 Hz pulsar at 2.5 kpc	$\Omega_0 \leq 4.4 \times 10^{-6}$

Table 2: Projected sensitivities to various GW sources, based on the S5 interferometer noise spectra. The inspiral horizon distances and luminosities correspond to the effective sensitivity of the interferometer array during the first calendar year of S5; L_{10} is 10^{10} times the blue light luminosity of the Sun. Note that because the horizon is the maximum detection distance, the effective search volume radius is approximately $\sqrt{5}$ times smaller than the horizon distance. The un-modeled burst energies assume isotropic emission, concentrated around 150 Hz. The pulsar and stochastic background sensitivities are the levels at which a 90% confidence level upper limit could be set, projected for 1 year of data (the stochastic limit assumes a Hubble constant of 72 km/sec/Mpc).

whether the gravitational waveforms can be accurately modeled or whether only less specific spectral characterizations are possible. Table 2 gives the sensitivity of the S5 instruments to various GW sources, and reference (20) contains all the LIGO observational publications.

The best understood transient sources are the final stages of binary inspirals (21), where each component of the binary may be a neutron star (NS) or a stellar-mass black hole (BH). GWs emitted by these systems release gravitational potential energy, moving the objects closer together and increasing the frequency of their orbit. The final stages occur rapidly, with the system sweeping in frequency across the LIGO band in a few to tens of seconds, depending on the mass of the system. The waveform can be calculated with reasonable precision and depends on a relatively small number of parameters. The analysis is done by matched-filtering the data for a set of waveforms that span a chosen parameter space. We characterize the astrophysical

reach for inspirals in terms of the "horizon", the distance at which an optimally oriented and located binary system would be detected, using matched filtering, with an amplitude signal-to-noise (SNR) ratio of 8. The horizon distance defines a volume in the universe, and the blue-light luminosity of galaxies within that volume is believed to be a good tracer of the compact binary population (22). Therefore we also characterize the astrophysical reach in terms of the total blue luminosity in the search volume; horizon distances and luminosities for two systems with masses representative of NS-NS and BH-BH systems are given in Table 2. Our own Milky Way galaxy has roughly 1.7×10^{10} blue solar luminosities, so for NS-NS inspirals, the search covers approximately 150 galaxies like our own.

Other astrophysical systems, such as core-collapse supernovae (23), black-hole mergers, and neutron star quakes, may produce GW bursts that can only be modeled imperfectly, if at all. When optimal filtering is not feasible, such bursts may still be detected, albeit at reduced sensitivity, using methods that identify excess power in the GW data streams and/or transient correlations between data from different detectors. The detectability of a particular GW burst signal depends primarily on the frequency content and duration of the signal, and the astrophysical reach can be characterized by the distance that a given energy emission in gravitational waves might be detected.

An example of a continuous source of GWs with a well-modeled waveform is a spinning neutron star (e.g., a pulsar) that is not perfectly symmetric about its rotation axis (24). The GWs will be sinusoidal with a very slowly decreasing frequency due to energy loss. If the neutron star is observed as a radio pulsar then the frequency and rate of change of frequency will be known; otherwise, a bank of templates will be needed to search over these parameters. For these sources, the astrophysical reach is the minimum equatorial ellipticity ϵ that could be detected at a typical galactic distance.

Processes operating in the early universe could have produced a background of GWs that is

continuous but stochastic (25). The astrophysical reach for such a background is characterized in terms of the spectrum $\Omega_{\rm GW}(f) = (f/\rho_{\rm c})(d\rho_{\rm GW}/df)$, where $d\rho_{\rm GW}$ is the energy density of GWs contained in the frequency range f to $f + df$, and $\rho_{\rm c}$ is the critical energy density of the Universe. Searches for such a background are performed by cross-correlating the outputs of a pair of detectors, typically assuming a constant frequency spectrum $\Omega_{\rm GW}(f) = \Omega_0$. Using the strain power spectra of two detectors, we can evaluate the minimum value of Ω_0 that would be detected with a given confidence level over a given integration time.

In addition to the GW channel, all searches rely on a host of ancillary signals to distinguish instrumental artifacts from potential GW signals. These channels monitor both the instrument (dozens of non-GW degrees-of-freedom) and its environment (magnetic fields, seismic and acoustic vibrations, etc.).

Networks and collaborations. Although in principle LIGO can detect and study GWs by itself, its potential to do astrophysics can be quantitatively and qualitatively enhanced by operation in a more extensive network. For example, the direction of travel of the GWs and the complete polarization information carried by the waves can only be extracted by a network of detectors. Early in its operation, LIGO joined with the GEO project, a German-British project operating a 600 m long interferometer near Hannover (26). Although with its shorter length the GEO 600 detector is not as sensitive as the LIGO detectors, for strong sources it can provide added confidence and directional/polarization information.

In May 2007, the Virgo detector began observations; a French-Italian project, the Virgo detector is similar to LIGO's, with 3 km arms (27). The LIGO Scientific Collaboration and the Virgo Collaboration have negotiated an agreement that provides that all data collected from that date will be analyzed and published jointly. This agreement is hoped to serve as the model for an eventual world-wide network.

Future directions. From its inception, LIGO was envisioned not as a single experiment, but as an on-going observatory. The facilities and infrastructure construction were specified, as much as possible, to accommodate detectors with much higher sensitivity, as experience and technology come together to enable improvements.

We have identified a set of relatively minor improvements to the current instruments (28) that can yield a factor of 2 increase in strain sensitivity and a corresponding factor of 8 increase in the probed volume of the universe. These improvements will be implemented following the end of S5, followed by another one-to-two year science run.

Even greater sensitivity improvements are possible with more extensive upgrades. Advanced LIGO will replace the interferometers with significantly improved technology, to achieve a factor of at least 10 in sensitivity (a factor of 1000 in volume) over the initial LIGO interferometers and to lower the seismic wall frequency down to 10 Hz (29), (30). Its operation will transform the field from GW detection to GW astrophysics. Advanced LIGO has been approved for construction by the National Science Board and is waiting to be funded. Installation of Advanced LIGO could start as early as mid-2010.

References

1. J. M. Weisberg, J. H. Taylor, in *Binary Radio Pulsars*, F. Rasio and I. Stairs, Eds. (Astronomical Society of the Pacific, San Francisco, 2005), p. 25.

2. A. Abramovici, *et al.*, Science **256**, 5325 (1992).

3. C. Cutler, K. S. Thorne, in *Proceedings of GR16*, N. T. Bishop and S. D. Maharaj, Eds. (World Scientific, Singapore, 2002).

4. Homepage of the LIGO Scientific Collaboration, http://www.ligo.org

5. A nice introduction to interferometric detector design is: P. Saulson, *Fundamentals of Interferometric Gravitational Wave Detectors* (World Scientific, Singapore, 1994).

6. R. L. Savage, Jr., P. J. King, S. U. Seel, Laser Phys. **8**, 679 (1998).

7. C. J. Walsh, A. J. Leistner, J. Seckold, B. F. Oreb, D. I. Farrant, Appl. Opt. **38**, 2870 (1999).

8. D. Ottaway, J. Betzwieser, S. Ballmer, S. Waldman, W. Kells, Opt. Lett. **31**, 450 (2006).

9. J. Giaime, P. Saha, D. Shoemaker, L. Sievers, Rev. Sci. Instrum. **67**, 208 (1996).

10. C. Hardham, *et al.*, Class. Quantum Grav. **21**, S915 (2004).

11. R. Adhikari, Ph. D. thesis, Massachusetts Institute of Technology (2004).

12. A. Dietz, *et al.*,"Calibration of the LIGO Detectors for S4" (LIGO Tech. Rep. T050262, 2006; http://www.ligo.caltech.edu/docs/T/T050262-01.pdf).

13. P. Fritschel, *et al.*, Appl. Opt. **37**, 6734 (1998).

14. S. Ballmer *et al.*, "Thermal Compensation System Description" (LIGO Tech. Rep. T050064, 2005; http://www.ligo.caltech.edu/docs/T/T050064-00.pdf).

15. B. J. Meers, Phys. Rev. D **38**, 2317 (1988).

16. D. Sigg, Ed., "Frequency Response of the LIGO Interferometer" (LIGO Tech. Rep. T970084, 1997; http://www.ligo.caltech.edu/docs/T/T970084-00.pdf).

17. P. R. Saulson, Phys. Rev. D **42**, 2437 (1990).

18. G. González, Class. Quantum Grav. **17**, 4409 (2000).

19. G. M. Harry *et al.*, Class. Quantum Grav. **19**, 897 (2002).

20. Links to all published observational results from LIGO can be found at http://www.lsc-group.phys.uwm.edu/ppcomm/Papers.html

21. K. Belczynski, V. Kalogera, T. Bulik, Astrophys. J. **572**, 407 (2002).

22. E. S. Phinney, Astrophys. J. **380**, 117 (1991).

23. H. Dimmelmeier, J. A. Font, E. Müller, Astrophys. J. Lett. **560**, L163 (2001).

24. P. Jaranowski, A. Królak, B.F. Schutz, Phys. Rev. D **58**, 063001 (1998).

25. M. Maggiore, Phys. Rep. **331**, 283 (2000).

26. H. Lück *et al.*, Class. Quantum Grav. **23** S71 (2006).

27. F. Acernese *et al.*, Class. Quantum Grav. **23** S635 (2006).

28. R. Adhikari, P. Fritschel, S. Waldman, "Enhanced LIGO" (LIGO Tech. Rep. T060156, 2006; http://www.ligo.caltech.edu/docs/T/T060156-01.pdf).

29. P. Fritschel, in *Gravitational-Wave Detection*, M. Cruise, P. Saulson, Eds. (SPIE Proc., 2003), vol. 4856, p. 282.

30. "Advanced LIGO Reference Design" (LIGO Tech. Rep. M060056, 2007; http://www.ligo.caltech.edu/docs/M/M060056-08/M060056-08.pdf).

31. The authors gratefully acknowledge the support of the United States National Science Foundation for the construction and operation of the LIGO Laboratory and the Particle Physics and Astronomy Research Council of the United Kingdom, the Max-Planck-Society and the State of Niedersachsen/Germany for support of the construction and operation of the GEO 600 detector. The authors also gratefully acknowledge the support of the research

by these agencies and by the Australian Research Council, the Natural Sciences and Engineering Research Council of Canada, the Council of Scientific and Industrial Research of India, the Department of Science and Technology of India, the Spanish Ministerio de Educacion y Ciencia, The National Aeronautics and Space Administration, the John Simon Guggenheim Foundation, the Alexander von Humboldt Foundation, the Leverhulme Trust, the David and Lucile Packard Foundation, the Research Corporation, and the Alfred P. Sloan Foundation.